JOURNAL OF CATALYSIS **179,** 597–605 (1998)
ARTICLE NO. CA982220

On the Crystal Structure and Cation Valence of Mn in Mn-Substituted Ba-β-Al_2O_3[1]

Maurizio Bellotto,*[,2] Gilberto Artioli,† Cinzia Cristiani,* Pio Forzatti,* and Gianpiero Groppi,*[,3]

*CIIC, Dipartimento di Chimica Industriale e Ingegneria Chimica "G. Natta," Politecnico di Milano, Piazza Leonardo da Vinci 32, 20133 Milan, Italy; †Dipartimento di Scienza della Terra, Università di Milano, 20133 Milan, Italy

Received March 23, 1998; revised June 26, 1998; accepted July 2, 1998

$BaMn_xAl_{12-x}O_{19-\alpha}$ combustion catalysts with $x = 0.5$, 1.0, 2.0, 3.0 have been investigated. The crystal structure and, specifically, the partitioning and the dominant oxidation state of Mn in the different crystallographic sites has been clarified by means of X-ray absorption spectroscopy and X-ray powder diffraction structure refinements of multiple diffraction powder data sets collected with both synchrotron and Cu-Kα radiation at different wave lengths in proximity and far from the Mn K adsorption edge. The results show that at low loading (up to $x = 1$) Mn preferentially enters tetrahedral Al(2) sites of Ba-β_I-Al_2O_3 as divalent cation. The occupancy of Ba sites in the mirror planes acts as a charge compensation mechanism to balance substitution of Al^{3+} with Mn^{2+}. At high Mn loading ($x \geq 1$) the occupation of Ba sites reaches unity and Mn preferentially enters octahedral Al(1) sites as Mn^{3+}. Surface area measurements and catalytic activity tests in CH_4 combustion have also been performed. The results indicate that the incorporation of Mn in the octahedral Al(1) sites causes reduction of surface area and has no beneficial effect on catalytic activity.

Key Words: **crystal structure; Mn valence; Mn-substituted hexaaluminates.**

INTRODUCTION

Mn-substituted hexaaluminates (1) are considered suitable catalysts for gas turbine applications in view of their high thermal stability and good combustion activity (2). These materials show stable phase composition up to 1600°C and high sintering resistance: they retain surface areas of 15–20 m^2/g upon calcination at 1300°C. This last property arises from anisotropic crystal growth of plate-like crystallites with large aspect ratio. The layered structure of these materials consists of alternate stacking along the *c* axis of Al^{3+}-containing spinel blocks and mirror planes in which large divalent and/or trivalent cations are located. Depending on the composition and the defectivity of the mirror plane, β-Al_2O_3 or magnetoplumbite-like structures are obtained. Measurements of anisotropic diffusion of oxide ions showed a reduced ion diffusion rate along the *c* axis (3). Thus a limited ability of rearrangement of the stacking pattern is observed that causes a preferential exposure of the mirror planes at the surface and prevents coalescence of the crystallites along the *c* axis (4). A detailed crystallographic picture for unsubstituted Ba-β-Al_2O_3 was derived from refinement analysis of single crystal and powder diffraction patterns (4-6). The existence of two different phases depending on the Ba content was demonstrated. The β_I Ba-poor phase has composition $Ba_{0.75}Al_{11}O_{17.25}$ that corresponds to the ideal Na-β-Al_2O_3 ($NaAl_{11}O_{17}$) in which, to maintain electroneutrality, a quarter of Ba^{2+} in Beevers–Ross sites are replaced by O^{2-} through a Reidinger defect mechanism; the other is a Ba-rich β_{II} phase of composition $Ba_{1.167}Al_{10.667}O_{17.167}$ in which Ba ions are located in both spinel blocks and mirror planes. Macroscopically monophasic samples are obtained also for intermediate composition, i.e. $BaAl_{12}O_{19}$, whose crystallites originate from intergrowth of β_I and β_{II} domains.

So far the crystal structure of Mn-substituted materials has not been fully clarified. Smets and Verlijsdonk (7) observed that incorporation of Mn in Ba-rich samples results in the formation of the β_I phase and in the segregation of $BaAl_2O_4$. Arai and co-workers (1) reported that monophasic samples are obtained for $BaMn_xAl_{12-x}O_{19-\alpha}$ up to $x = 2$ and segregation of $BaAl_2O_4$ occurs upon further Mn addition. Smets and Verlijsdonk (7) observed a strong analogy between Mn and Mg-doped Ba-β-Al_2O_3, suggesting that Mn is located in the spinel blocks as Mn^{2+}. Along these lines, further ESR studies of Na-β-Al_2O_3-doped single crystals confirmed that Mn is located in the spinel blocks, predominantly as Mn^{2+} in the tetrahedral Al(2) site (8). Moreover, similar Mn localisation is reported for ammonium beta aluminate (9). Finally the structural analysis of barium hexaaluminate single crystals substituted with low Mn content

[1] Paper presented at the 3rd International World Conference on Catalytic Combustion (IWCC), Amsterdam, The Netherlands, September 23–25, 1996.

[2] Present address CTG, Rue des Technodes, 78931 Guerville Cedex, France.

[3] To whom correspondence should be addressed. E-mail: gianpiero.groppi@polimi.it.

0021-9517/98 $25.00

indicated that in this case also Mn is located in the Al(2) site (3). Thus, the incorporation of small divalent ions in substitution of Al^{3+} in tetrahedral Al(2) sites appears to be a common feature of β-Al_2O_3 materials. Similarly the location of divalent ions in magnetoplumbite related structure are reported in several papers (10, 11).

What reported so far typically refers to materials doped with small amounts of Mn. Few studies have been published concerning the effect of the addition of large amount of Mn. This issue is obviously relevant to the use of these materials as combustion catalysts since Mn is responsible for the catalytic properties, so that a significant concentration of this ion is desired. Recently Arai and co-workers published a study on the effect of Mn concentration in $SrMn_yAl_{12-y}O_{19}$, a system that exhibits a magnetoplumbite structure (12). Two distinct phases have been obtained upon addition of Mn above $y = 0.5$. Partial substitution of Sr^{2+} with Pr^{3+} was shown to increase the amount of Mn incorporated in the structure without phase separation. A charge compensation effect allowing for the substitution of Al^{3+} with Mn^{2+} was hypothesised but no specific evidences were provided.

In this work we have investigated the Mn localisation and its valence at the different sites in substituted Ba-β-Al_2O_3 with different Mn/Ba ratios varying from 0.5 to 3. Rietveld refinements of multiple sets of X-ray diffraction powder data collected at different wave lengths in proximity and far from the Mn K adsorption edge with both synchrotron and Cu-Kα radiation have been used for this purpose. Catalytic activity in CH_4 combustion has been also investigated. These data are discussed in connection to the crystallographic analysis with the aim to rationalise the catalytic properties of these materials.

METHODS

Four Mn-substituted Ba-β-Al_2O_3 samples with nominal composition $BaMn_xAl_{12-x}O_{19}$ ($x = 0.5$, 1, 2, and 3) have been prepared via co-precipitation in aqueous medium. Soluble nitrate salts of the constituents and $(NH_4)_2CO_3$ as a precipitating agent have been used as raw materials (13). The precursor materials have been obtained upon filtration, washing, and overnight drying at 110°C. The following calcination procedure has been performed in order to obtain the final materials: from room temperature up to 1300°C with heating rate 60°C/h and hold at 1300°C 10 h. To evaluate the thermal evolution of the systems intermediate steps at 700, 900, 1000, 1100, and 1200°C have been realised (hold at 700 and 1000°C 10 h and at the other steps 1 h). The calcined samples are quoted in the following with notations referring to the nominal Mn/Ba ratio and the calcination temperature (e.g. BaMn0.5–1200 indicates the sample with expected composition $BaMn_{0.5}Al_{11.5}O_{19}$ calcined at 1200°C).

Chemical analyses of the mother liquors and of the samples calcined at 1300°C have been performed by atomic absorption. The results confirm that quantitative precipitation is obtained and that the measured final compositions correspond to the expected ones.

Surface areas have been measured by nitrogen adsorption using a Fison Sorptomatic 1900 series instrument.

EPR spectrum of BaMn0.5 has been collected by a Varian E109 spectrometer.

The X-ray powder diffraction patterns (XRD) of all the Mn-substituted β-aluminas have been measured using Cu-Kα radiation and a pyrolitic graphite diffracted beam monochromator (Philips vertical diffractometer PW 1050-70). The data have been collected in the angular range 5°–120° 2θ.

The anomalous diffraction synchrotron powder data necessitate of an experimental reference for the scattering coefficients of Mn^{2+} and Mn^{3+} in a local coordination similar to that of the investigated samples. For this purpose a Mn_3O_4 synthetic Hausmannite sample has been chosen as standard. The X-ray absorption of all the BaMnX samples along with that of the reference Mn_3O_4 has been first measured to calibrate the energy position of the Mn-K absorption edge. Then, for the BaMn1.0 and BaMn2.0 samples, as well as for the reference sample, the X-ray powder patterns have been measured at three wavelengths in proximity of the Mn-K edge, approximately at −20 eV, −50 eV, and −200 eV from the Mn edge position defined as the maximum of the first derivative peak of the absorption curve. The spectra have been collected using synchrotron radiation at line 2.3 of SRS, Daresbury laboratory. The monochromatic incident beam was obtained using a Si(111) monochromator.

The powder diffraction patterns have been used in a Rietveld refinement using the GSAS software (14). Both Cu-Kα and synchrotron radiation patterns have been used in multipattern refinements in the case where several diagrams were measured for the same sample. Anisotropic peak broadening along the (001) zone axis was included in the refinements of the Lorenzian part of the pseudo-Voigt function for the Mn-substituted Ba-β-Al_2O_3 to model their plate-like particle shape.

For BaMn1.0, BaMn2.0 and for the reference sample, Mn_3O_4, independent Mn f' site-resolved anomalous scattering coefficients have been refined for all the sites with sufficient Mn occupancy. All the four collected patterns (Cu-Kα, −20 eV, −50 eV, and −200 eV) have been simultaneously refined but Mn f′ values have been refined only for the synchrotron data collected closer to the Mn K absorption edge (−20 eV and −50 eV). For all the other diagrams and when the Mn occupancy was lower than 0.05, the f′ coefficients have been fixed at the ideal values calculated by the FPRIME program (15) for Mn° and corrected for the proper consideration of the Mn^{2+} and Mn^{3+} chemical shift.

Catalytic activity measurements have been performed in a quartz microreactor (ID 0.8 cm) filled with fine

catalyst powders (dp < 0.1 mm) to minimise diffusive limitations. Catalyst powders have been diluted with quartz ($V_{ctz}/V_{quartz} = 2/1$) with the same particle size. A feed composition of 1% v/v of CH_4 in air has been adopted as representative of catalytic combustion under large excess of oxygen that is typical of gas turbine operations (1). Dilution of catalyst and relatively low CH_4 concentration allow for small temperature gradients in the reactor below 20% conversion. In all the experiments GHSV have been fixed to 48000 h^{-1}. The reactor was equipped with a sliding thermocouple (chromel–alumel) that allowed for the measurement of axial *T*-profiles. The analysis of products and reactants have been performed by on-line gas chromatography. Further details on the experimental setup are reported elsewhere (13).

RESULTS

Phase Composition

The X-ray powder diffraction spectra of the BaMn0.5, BaMn1.0, BaMn2.0 samples calcined at 1300°C show the presence of a single Ba-β-Al_2O_3 phase only. On the contrary the BaMn3.0 sample retains a small fraction of $BaAl_2O_4$. This latter is an intermediate phase in the synthesis of all the samples (13). In the case of BaMn0.5, BaMn1.0, and BaMn2.0, $BaAl_2O_4$ appears at temperatures ranging from 900 to 1000°C and disappears between 1100 and 1200°C when the final Ba-β-Al_2O_3 phase is formed. In the case of BaMn3.0, $BaAl_2O_4$ appears already at 700°C but persists up to 1400°C in line with literature reports (1).

X-Ray Absorption near Edge Spectroscopy (XANES)

The Mn XANES spectra measured over all Mn-substituted Ba-β-Al_2O_3 samples and over the Mn_3O_4 reference sample are shown in Fig. 1. The literature spectrum (16) of $MnCr_2O_4$ is also reported. The Mn K edge has been evaluated as the maximum of the first derivative curve in the Mn_3O_4 standard ($E = 6544$ eV). The edge is at about the same value in samples BaMn2.0 and BaMn 3.0, whereas it is shifted at slightly lower energies in samples BaMn1.0 and BaMn0.5. These values compare well with those reported by Kohm *et al.* (17) for Mn^{2+}. Qualitative comparison of the near edge features indicate that a progressive shift from Mn^{2+} to higher oxidation states occurs in Mn-substituted Ba-β-Al_2O_3 on increasing the Mn content, based on the following observations: (1) the first structure on the edge (at about 6547 eV) is well evident in the $MnCr_2O_4$ literature spectrum and in the BaMn0.5 and BaMn1.0 samples, whereas it progressively decreases and reduces to a small shoulder in the other spectra; (2) the pre-edge peaks at about $E = 6538$ eV, characteristic of tetrahedral Mn^{2+} (18), in samples BaMn0.5 and BaMn1.0 are at the same energy of the prepeak in the $MnCr_2O_4$ literature spectrum, whereas the peak is much smaller and slightly shifted to higher energy in the other spectra; (3) the white peak is at about $E = 6554$ eV in the case of $MnCr_2O_4$ spectrum, BaMn0.5, and BaMn1.0 samples, again the white peak gradually shifts towards higher energy (at about $E = 6557$ eV) in the other samples. All these features reflect an increase in the Mn oxidation state. As a whole the XANES diagrams of the Mn-substituted Ba-β-Al_2O_3 samples suggest that Mn is almost entirely present as Mn^{2+} in BaMn0.5, while a significant fraction of trivalent and/or tetravalent Mn is present in BaMn2.0 and BaMn3.0. Sample BaMn1.0 shows intermediate features.

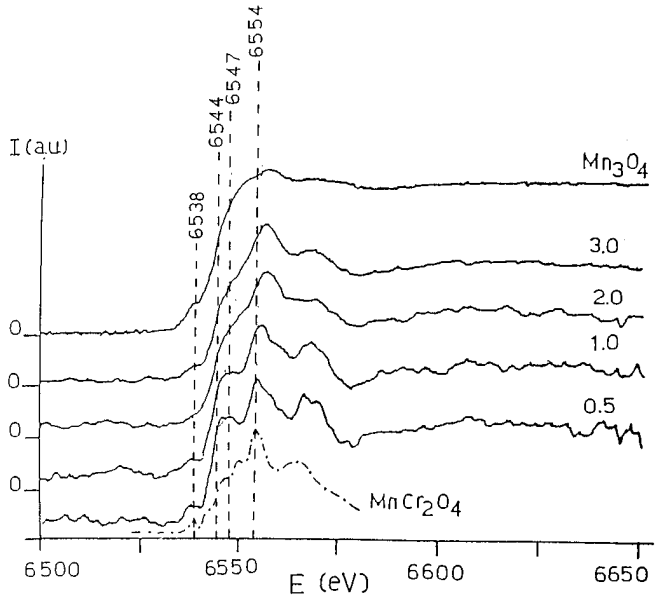

FIG. 1. X-ray absorption spectra of BaMn*X* samples, reference Mn_3O_4, and literature $MnCr_2O_4$.

The dominant divalent state of Mn at low concentration has been confirmed by EPR measurements performed over BaMn0.5 that exhibits a strong unresolved EPR signal associated with Mn^{2+} species.

Structural Analysis

Based on the XRD data, the Ba-β_I-Al_2O_3 structure (4) has been chosen for all the samples as starting model for the Rietveld refinements. In Fig. 2 the ideal semicell of Ba-β_I-Al_2O_3 (A) is reported along with the description of a Reidinger defect (B) associated with a Ba vacancy that occurs due to electroneutrality reasons. The Reidinger mechanism implies the presence of an additional O^{2-} ion in the mirror plane with a related shift of Al sites from Al(1) to Al(5) positions. The constraints on site occupancies relevant to the Reidinger mechanism are reported in Table 2.

The results of Rietveld analysis confirm that a Ba-β_I-Al_2O_3 phase indeed formed in all the samples despite the large amount of Ba, in line with previous literature reports (7). Refinements of the Al occupancies and the analysis of

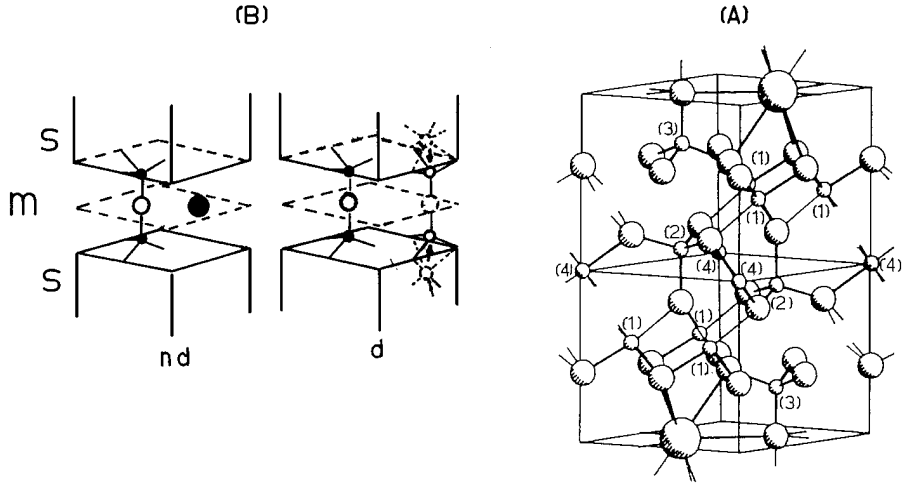

FIG. 2. (A) Ideal semicell (numbers in parenthesis refer to the different Al sites); (B) Reidinger defects of Ba-β_1-Al_2O_3 (nd = nondefective cell, d = defective cell, s = spinel blocks, m = mirror planes, bold small sphere = Al in regular position Al(1), bold large sphere = Ba, open large sphere = oxygen in regular position in the mirror plane O(5), open small sphere = Al shifted from regular Al(1) to interstitial position Al(5), dashed large sphere = interstitial oxygen replacing Ba ion).

difference Fourier maps readily indicate the presence of Mn in the tetrahedral Al(2) sites. At the same time the Ba occupancy increases to reach unit for BaMn2.0 and BaMn3.0. Thus, the absence of Reidinger defects has been imposed for these two samples, while for all the samples Mn has been introduced in the Al(2) sites constrained to unit occupancy. Further refinements of the Al(1), Al(3), and Al(4) occupancies indicate the presence of Mn in the Al(1) sites for the higher Mn content, while Al(3) and Al(4) do not show any significant evidence of Mn substitution. Accordingly for all the samples Mn has been allowed in the Al(1) and Al(2) sites only, again with the constraint of total site occupancy. In BaMn0.5 and BaMn1.0 Al(1) occupancy shall nevertheless account for the possible presence of Reidinger defects. The Mn-content determined by these refinements does not account for the total amount present in the samples as determined by chemical analysis, the discrepancies being larger with increasing the Mn content. However, the difference Fourier maps do not indicate any possible alternative location for the Mn not accounted for. Consequently the Mn/Ba ratios have been fixed to the known values, and further refinements have been performed with the constraint on the total Mn amount, Mn being still limited to the Al(1) and Al(2) sites.

At this stage the refinement of the anomalous dispersion Mn f' values has been released according to the procedure described in the Experimental section. This procedure assures the internal consistency of the data and reduces the correlation between the occupancy and the f' values. The main results of these final refinements of the powder diffraction patterns are summarised in Tables 1 and 2. In particular, the calculated composition reported in Table 1 has been

TABLE 1

Results of Structural Refinement on Samples $BaMn_xAl_{12-x}O_{19}$

Results	Samples			
	BaMn0.5	**BaMn1.0**	**BaMn2.0**	**BaMn3.0**
χ^2	1.362	1.755	1.237	0.601
Phase composition	Ba-β-Al_2O_3	Ba-β-Al_2O_3	Ba-β-Al_2O_3	Ba-β-Al_2O_3 $BaAl_2O_4$ (2%w/w)
$\mathbf{a_0 = b_0}$ **(Å)**	5.6176(3)	5.64123(4)	5.65916(3)	5.6719(1)
$\mathbf{c_0}$ **(Å)**	22.739(1)	22.7260(3)	22.7429(2)	22.776(1)
Expected composition	$BaMn_{0.5}Al_{11.5}O_{19}$	$BaMn_1Al_{11}O_{19}$	$BaMn_2Al_{10}O_{19}$	$BaMn_3Al_9O_{19}$
Calculated composition	$BaMn_{0.46}Al_{12.79}O_{20.71}$	$BaMn_{1.0}Al_{12.14}O_{20.45}$	$BaMn_2Al_9O_{17}$	$BaMn_3Al_8O_{17}$
Calculated (Al + Mn)/Ba	13.23	13.15	11	11

Note. All cell parameters refer to Ba-β-Al_2O_3.

TABLE 2

Refined Sites Occupancy in Ba-β-Al_2O_3 of Samples $BaMn_xAl_{12-x}O_{19}$-1300

Atom	Site symm.	Mult.	Site occupancy			
			BaMn0.5	BaMn1.0	BaMn2.0	BaMn3.0
Ba(1)	6m2	2	0.829(5)	0.839(4)	1.00	1.00
Al(1)	m	12	0.937(2)	0.928(1)	0.867(3)	0.724(7)
Al(2)	3m	4	0.810(1)	0.646(5)	0.399(8)	0.33(2)
Al(3)	3m	4	1.00	1.00	1.00	1.00
Al(4)	3m	2	1.00	1.00	1.00	1.00
Al(5)	m	12	0.057(2)	0.054(1)	0.00	0.00
Mn in Td Al(2) site	3m	4	0.19(1)	0.354(5)	0.601(5)	0.67(2)
Mn in Oh Al(1) site	m	12	0.00	0.023(2)	0.133(3)	0.276(7)
O(1)	m	12	1.00	1.00	1.00	1.00
O(2)	m	12	1.00	1.00	1.00	1.00
O(3)	3m	4	1.00	1.00	1.00	1.00
O(4)	3m	4	1.00	1.00	1.00	1.00
O(5)	6m2	2	1.00	1.00	1.00	1.00
O(6)	mm2	6	0.057(2)	0.054(1)	0.00	0.00

Note. Constraints on occupancies relevant to reidinger defect mechanism. $Ba(1) + 3Al(5) = 1$; $Al(5) = O(6)$; $Al(5) + Al(1)^a = 1$. (^{a} Mn occupancy in Al(1) must be included.)

obtained on the basis of the values of the site occupancy and multiplicity reported in Table 2.

The atomic content of Mn in the Al sites of a semicell is reported in Fig. 3 as a function of the expected Mn/Ba ratio. At low content Mn enters only in the Al(2) sites with an occupancy that increases almost linearly with Mn loading. For Mn/Ba > 1 the Mn occupancy in the Al(2) sites tends to an asymptotic value slightly higher than 0.5 (see Table 2), whereas an increasing amount of Mn is found in the Al(1) sites. A gradual rise of the occupancy of the Ba sites in the mirror plane for Mn/Ba ratios <1 parallels the increase of Mn occupancy in the Al(2) sites up to the disappearance of the Reidinger defects. Considering that the presence of one Ba^{2+} ion in the mirror plane instead of one O^{2-} ion (i.e. disappearance of a Reidinger defect) implies 4+ charge variation. Such an evidence suggests the occurrence of a charge compensation mechanism that is based on the progressive decrease of Reidenger defects to balance substitution of Al^{3+} with divalent Mn in the Al(2) sites.

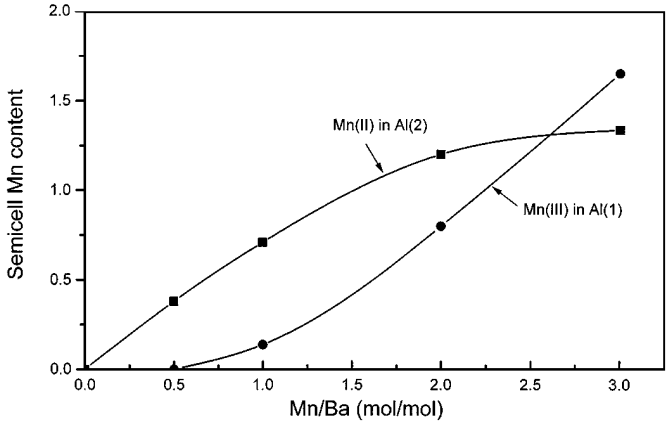

FIG. 3. Calculated atomic content of Mn in the Al sites of a semicell.

According to the theory of resonant X-ray diffraction at all wavelengths above the absorption edge the f' anomalous dispersion coefficient of divalent Mn is always smaller than the f' value of trivalent Mn, the difference becoming vanishingly small far from the absorption edge. This feature has been employed to resolve valence ambiguities between cation sites when different oxidation state of the element of interest are partitioned over distinct crystallographic sites (19–21). The refined f' coefficients for the reference Mn_3O_4 sample, reported in Table 3, along with the theoretical values and the refined values of BaMn1.0 and BaMn2.0, illustrate the method. Hausmannite has the direct spinel structure with complete partitioning of Mn^{2+} in the tetrahedral sites and Mn^{3+} in the octahedral ones. The results are in agreement with the expectation of the f' values for divalent Mn being markedly smaller than those of trivalent Mn ones. In line with previous literature reports (21) the difference between the experimental values of Mn^{2+} and Mn^{3+} f' coefficients is larger than that expected from theory of resonant X-ray diffraction.

The refinements of BaMn2.0 show that the Mn f' values calculated for the Al(2) sites are lower than that obtained for the Al(1) ones. Deviations from the theoretical values are in line with experimental and theoretical uncertainties

TABLE 3

Theoretical and Refined f' values at −20 and −50 (eV) for Isolated Mn Ions, Reference Mn_3O_4, BaMn1.0, and BaMn2.0)

f' values	−20 (eV)	−50 (eV)
Theoretical for isolated ions		
Mn(II)	−5.587	−4.613
Mn(III)	−5.422	−4.545
Refined for reference Mn_3O_4		
Mn(II) Td	−5.84(2)	−4.75(2)
Mn(III) Oh	−5.34(2)	−4.48(2)
Refined for		
BaMn1.0		
Mn in Al(2)	−5.61(3)	−4.2(3)
Mn in Al(1)	−5.422	−4.545
BaMn2.0		
Mn in Al(2)	−5.9(2)	−4.8(2)
Mn in Al(1)	−4.8(7)	−4.6(6)

and the results indicate that Mn in Al(2) is predominantly divalent and Mn in Al(1) is mainly trivalent. On the other hand, the calculated Mn f' values in BaMn1.0 do not show such a clear trend. This is likely due to the low occupancy of Mn in the Al(1) sites that has not allowed refinement of the corresponding Mn f' values that, accordingly, have been fixed to the theoretical values for Mn^{3+}.

The calculated values of the a_0 lattice parameter and of the c_0/a_0 ratio versus Mn loading that are plotted in Figs. 4 and 5, respectively, support the attribution of the Mn valence in the different crystallographic sites derived from the f' refinements of BaMn2.0. The a_0 lattice parameter increases with the Mn loading in the whole investigated range, even though the rise is steeper up to Mn/Ba = 1 and it is less pronounced for higher Mn loadings. This behaviour is consistent with the initial substitution of Al(2) with divalent Mn ions which causes a marked expansion of the site coordination distance. Afterwards, on increasing further the

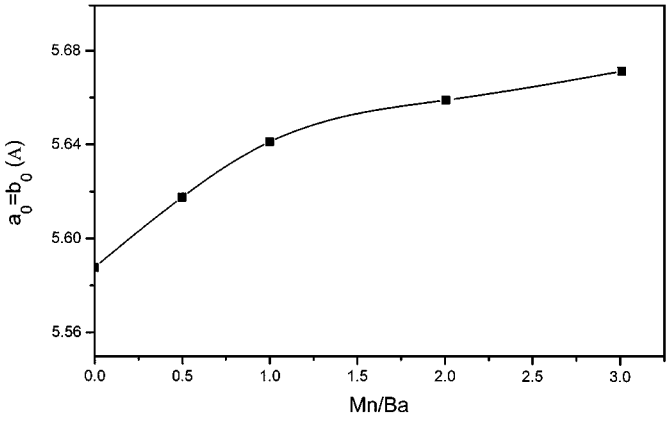

FIG. 4. Calculated $a_0 = b_0$ cell parameter as function of total Mn.

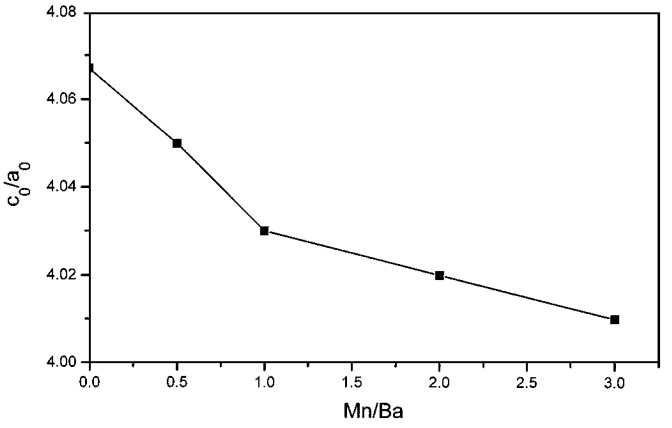

FIG. 5. Calculated c_0/a_0 ratio as function of total Mn.

Mn content, substitution of Al(1) with Mn^{3+} causes only minor site distortions due to close similarity between the ionic radii of Al^{3+} and Mn^{3+}. The trend of the c_0/a_0 ratio once more confirms the above interpretation. At low Mn content the c_0/a_0 ratio decreases almost linearly with the Mn loading. This behaviour quantitatively agrees with that reported in the literature for Mg-doped Ba-β-Al_2O_3 (7) and it can be explained as follows: the substitution of Al(2) with divalent Mn reduces the concentration of Reidinger defects, thus enforcing the bonds between the spinel block and the mirror plane which is thus contracted. This compensates for the expansion along the c axis due to incorporation of Mn^{2+} in the spinel blocks. For Mn/Ba > 1 Mn enters the Al(1) sites mainly as Mn^{3+} and no further increase of the Ba concentration is observed. Accordingly both c_0 and a_0 expand and their ratio keeps almost constant.

Also the average Al(x)-O distances reported in Fig. 6 support the attribution of the Mn valence in the different sites. The Al(2)-O distance markedly grows on increasing Mn content up to BaMn2.0 in line with progressive replacement

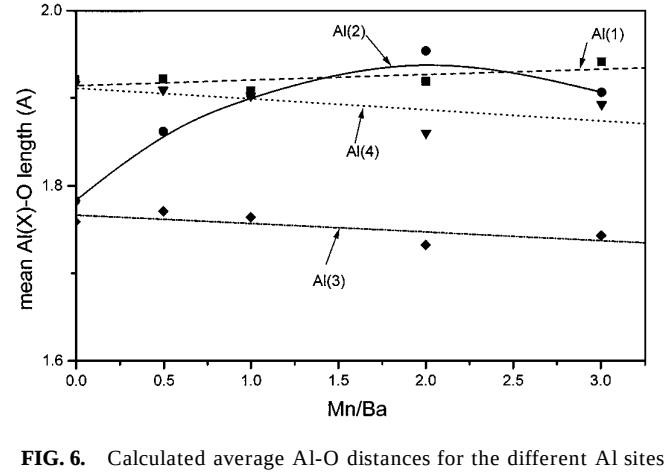

FIG. 6. Calculated average Al-O distances for the different Al sites as function of total Mn content.

TABLE 4

Surface Area of the $BaMn_xAl_{12-x}O_{19}$ Samples Calcined at 1300°C (10 h)

Sample	Surface area (m^2/g)
$BaAl_{12}O_{19}$	15
$BaMn_{0.5}Al_{11.5}O_{19}$	20
$BaMn_1Al_{11}O_{19}$	17
$BaMn_2Al_{10}O_{19}$	12
$BaMn_3Al_9O_{19}$	6

of Al^{3+} with larger Mn^{2+} ions. On the other hand, only small or negligible increase of the Al(1)-O distances is observed according to the presence of Mn ions at higher oxidation state with size closer to that of Al^{3+}. It is worth to observe that no significant changes occur with Mn content in the other Al(x)-O distances corresponding to sites where no Mn substitution has been found.

Morphology

The measured surface areas of $BaMn_xAl_{12-x}O_{19}$ samples calcined at 1300°C are listed in Table 4. The value for the Mn-free sample (BaAl12) refers to a previously investigated sample (4), prepared according to the same coprecipitation procedure adopted in this work. The results agree well with those reported in the literature for samples with the same composition prepared via hydrolysis of metal alkoxides (1). It is shown that Mn incorporation has only a minor effect on the surface area up to Mn/Ba = 1, whereas at higher Mn content the surface area gradually decreases with Mn loading.

Structure refinements allowed for the calculation of the aspect ratios of the anisotropic plate-like crystallites of Ba-β_I-Al_2O_3. In Fig. 7 the calculated values of the aspect ratio are plotted versus surface areas for the Mn-substituted samples and for two previously investigated unsubstituted Ba-β-Al_2O_3 (4) samples: one, with nominal composition $BaAl_{14}O_{22}$ consisting of a Ba-β_I-Al_2O_3 phase, isostructural to that of Mn-containing samples; the other, with nominal composition $BaAl_{12}O_{19}$ (i.e. with Ba/Al ratio equal to Ba/(Mn + Al) ratio in the investigated samples), consisting of an intergrowth between Ba-β_I-Al_2O_3 and Ba-β_{II}-Al_2O_3. Figure 7 shows that in the Mn-substituted samples the measured surface area and the calculated aspect ratio are almost linearly related, thus confirming that the sintering resistance arises from inhibition of the crystal growth along the *c*-axis associated with the anisotropic oxygen diffusion coefficients. Comparison with unsubstituted Ba-β-Al_2O_3 should account for the structural differences between Ba-β_I-Al_2O_3 and $BaAl_{12}O_{19}$. Ba-β_I-Al_2O_3, isostructural with the Mn-substituted samples, exhibits the lowest values of both surface area and crystallite aspect ratio, which correlate well with those of the Mn-containing samples. The worst morphological properties of the unsubstituted sample of composition $BaAl_{14}O_{22}$ could be related its lower Ba concentration. On the other hand, the $BaAl_{12}O_{19}$ sample exhibits values of surface area close to those of BaMn0.5 and BaMn1.0, but with a markedly higher aspect ratio. Such marked deviation from surface area versus aspect ratio correlation is possibly related to the peculiar microstructure of $BaAl_{12}O_{19}$ associated with the intergrowth of β_I and β_{II} domains.

Catalytic Activity

The results of catalytic activity tests in CH_4 combustion performed over the investigated Mn-substituted Ba-β-Al_2O_3 and over $BaAl_{12}O_{19}$ are reported in Fig. 8. The results compare very well with those already reported in the literature for samples with similar compositions (1). In particular the experimental curves show that up to Mn/Ba = 1 the conversion at a fixed temperature markedly grows on

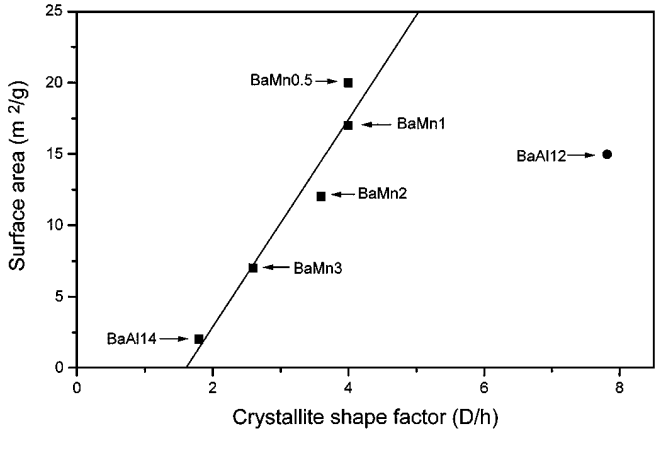

FIG. 7. Surface area vs calculated aspect ratio of crystallites.

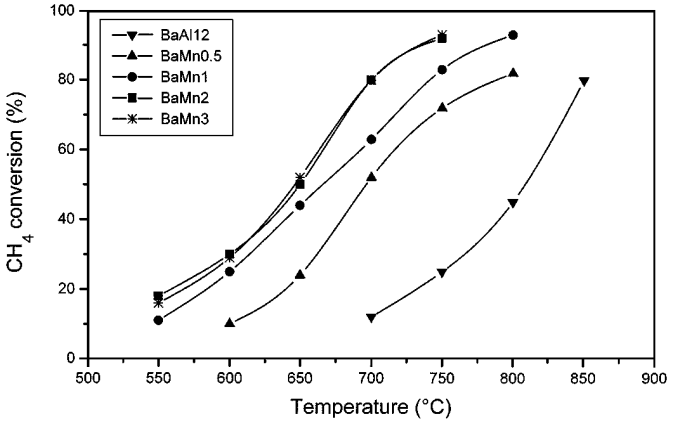

FIG. 8. Results of CH_4 combustion test over BaMnX and BaAl12 (operating conditions; see Experimental).

increasing the Mn loading. On the other hand, only a slight enhancement of conversion is obtained on increasing the Mn content from BaMn1.0 to BaMn2.0. No further enhancement of conversion is observed for BaMn3.0. Similar values of the apparent activation energy in the range 21–23 kcal/mol have been calculated from the conversion curves for all the Mn-containing samples.

DISCUSSION

The detailed crystallographic study on Mn-substituted Ba-β-Al_2O_3 herein reported has shown that, at low concentration, Mn preferentially enters the structure as Mn^{2+} in the tetrahedral Al(2) sites. The Al(2) sites in the unsubstituted Ba-β_I-Al_2O_3 structure (4) are larger and less distorted than the other Al sites and thus they are very likely better suited to host the larger and less positive Mn^{2+} ions.

Replacement of Al^{3+} by Mn^{2+} causes a decrease of the Reidinger defects. It is this mechanism of charge compensation that allows for insertion of a substantial amount of Mn in the Ba-β_I-Al_2O_3 structure without phase separation. This charge compensation mechanism is not allowed in the magnetoplumbite structure, where cation vacancies in the mirror planes are not present to a significant extent. Accordingly, elements at higher oxidation state (e.g., Pr^{3+}, La^{3+}) should be inserted in the mirror plane to allow allocation of divalent Mn in the spinel blocks (12).

On increasing the Mn content, Ba sites are progressively saturated and the Reidinger defects disappear. Accordingly, the charge compensation mechanism no longer exists and Mn preferentially enters the octahedral Al(1) sites as Mn^{3+}. However, at high Mn loadings the Mn occupancy in Al(2) sites slightly exceeds the value of 0.5 that, according to the charge compensation mechanism, corresponds to the saturation of Ba sites. Consequently, if all Mn in Al(2) is divalent and Mn in Al(1) is trivalent, electroneutrality is not respected. Thus, the presence of a small fraction of Mn^{3+} in Al(2) and/or of Mn^{4+} species has to be invoked to ensure the electroneutrality.

Identification of partitioning and of the dominant valence state of Mn in the different crystallographic sites as a function of the total Mn loading provides a basis for the discussion of the observed morphological and catalytic combustion properties. The correlation between the surface area and calculated aspect ratio of the crystallites confirms that the sintering resistance arises from inhibition of the crystal growth along the *c* axis due to oxygen anisotropic diffusion coefficients in the layered structure as already reported for Mn-free systems [4]. The data obtained at low Mn loading (up to Mn/Ba = 1) show that the substitution of Al^{3+} with divalent Mn in the Al(2) sites has a minor effect on the morphological properties. On the other hand, further Mn insertion in the Al(1) sites reduces both the surface area and the crystallite aspect ratio, thus suggesting that Mn promotes diffusion of Ba^{2+} (and O^{2-}) ions in the structure. The promoting effect of Mn on the diffusion of Ba^{2+} ions in the spinel blocks is also supported by the decreasing of the temperature required for the formation of the Ba-β_I-Al_2O_3 phase on increasing the Mn content. In fact, a previous study on Ba-Al-O systems prepared according to the same coprecipitation procedure herein adopted (22) shows that the formation of the Ba-β-Al_2O_3 phase occurs via a solid state reaction and requires diffusion of Ba-ions within β-Al_2O_3 spinel blocks. The absence of a significant effect on sintering at low Mn content could be related to the increase of Ba concentration in the mirror planes associated with the substitution of divalent Mn in tetrahedral Al(2). The increase of sintering resistance on increasing the Ba concentration in Ba-β-Al_2O_3 structure has been already reported for Ba-Al-O systems and could balance the Mn effect up to the saturation of the Ba sites (i.e., $x = 1.0$).

An attempt has been made to correlate the catalytic activity in CH_4 combustion to the different Mn species identified in the present study. For this purpose the values of the kinetic rate constants referred to unit weight (k_w) have been derived from the data assuming a first-order dependence on fuel concentration **and a plug flow isothermal behaviour of the reactor**. Then the turnover frequencies referred to the bulk content of the different Mn species have been calculated by dividing k_w by the number of Mn moles as derived from the refinements (TOF1). Another TOF value has been calculated by dividing the value of the TOF referred for the total Mn amount in the bulk by the specific surface area of the samples (TOF4). Notice that this latter value is related to the TOF referred to as the overall amount of Mn at the surface under the assumption that the surface concentration of Mn is proportional to the overall Mn content in the bulk. It is worth noticing that to allow for derivation of TOF values the kinetic constants have been calculated on a catalyst weight basis. On the other hand, GHSV in the experiments was kept constant on a catalyst bed volume basis for the sake of comparison with previous literature tests (1). Accordingly different k_w values arise from very close conversion curves due to variation of the apparent density of the catalyst bed.

The calculated values of k_w and TOF at 600°C are reported in Table 5. The values of k_w show that the activity referred to as the unit weight of the catalyst increases up to BaMn2.0 and slightly decreases with further increasing the Mn amount. The decrease of activity in BaMn3.0 is more evident if TOF1, referred to as the total content of Mn in the bulk, is considered. From the analysis of the data in Table 5 two alternative hypotheses can be derived to account for the activity drop. The values of TOF4 that keep almost constant on varying the Mn content indicate that this drop can be related to the decrease of surface area observed in BaMn3.0. On the other hand, the activity of BaMn*X* can also be related to the amount of Mn in Al(2) as suggested

TABLE 5

Specific Kinetics Constant Rates of BaMnx at 600°C

Sample	k_w (Nml/g/s)	TOF1 (s^{-1})	TOF2 (s^{-1})	TOF3 (s^{-1})	TOF4 (a.u.)
BaMn0.5	1.84	0.13	0.13	-	6.4×10^{-3}
BaMn1.0	4.68	0.16	0.20	1.01	9.7×10^{-3}
BaMn2.0	6.51	0.12	0.20	0.30	9.9×10^{-3}
BaMn3.0	4.18	0.053	0.12	0.095	8.8×10^{-3}

Note. Turn over frequencies: TOF1 referred to total Mn in the bulk; TOF2 referred to Mn in Al(2); TOF3 referred to Mn in Al(1); TOF4 referred to total Mn at the surface.

by the values of TOF 2 in Table 5, that, despite some scattering, are reasonably constant on varying the Mn content. At variance we have the following facts: (i) BaMn.05, in which Mn in Al(1) has not been found, possesses combustion activity, (ii) a marked drop of TOF3 is observed in the other samples on increasing the Mn content. These indicate that no correlation exists between the activity and Mn in Al(1).

From the results obtained in this work no definitive conclusions can be drawn in favour of one of the two hypotheses above. In any case it is apparent that substitution of trivalent Mn in Al(1) sites at high Mn loading does not effectively improve catalytic activity, possibly due to the low activity of this Mn species or to its promoting effect on sintering.

CONCLUSIONS

A detailed structure analysis by spectroscopic and diffraction methods taking advantage of the resonant scattering effect in the proximity of the Mn absorption K-edge has allowed the determination of partitioning and dominant valence state of Mn in the different crystallographic sites of Mn-substituted hexaaluminates.

At low concentration Mn preferentially enters the structure as Mn^{2+} in the tetrahedral Al(2) sites. The resulting charge variation is balanced by an increase of Ba concentration in the mirror planes through reduction of the number of Reidinger defects. Beyond saturation of Ba sites corresponding to a Mn occupancy in Al(2) site of 0.5, this charge compensation mechanism is no longer effective and Mn preferentially enters the structure as Mn^{3+} in octahedral Al(1) sites.

Analysis of the surface area and catalytic activity data on the basis of this crystallographic picture has shown that the replacement of Al with trivalent Mn in Al(1) sites without increase of Ba concentration in the mirror plane favour the sintering of the material. Moreover, such replacement does not improve catalytic activity. No clear evidence has been found to discriminate if this behaviour is due either to the low activity of this Mn species or to its promoting effect on sintering.

ACKNOWLEDGMENTS

Financial support for this work has been provided by MURST, Rome, Italy and by EC with Contract JOR3-CT96-0071 (DG12-WSME). Access to the SRS beam station was made possible by the EC Large Installation Plan. Thanks are also due to Professor Elio Giamello of Università di Torino for EPR measurements.

REFERENCES

1. Machida, M., Eguchi, K., and Arai, H., *J. Catal.* **120**, 386 (1989).
2. Arai, H., and Fukuzawa, H., *Catal. Today* **26**, 217 (1995).
3. Machida, M., Sato, A., Kijima, T., Inoue, H., Eguchi, K., and Arai, H., *Catal. Today* **26**, 239 (1995).
4. Groppi, G., Assandri, F., Bellotto, M., Cristiani, C., and Forzatti, P., *J. Solid State Chem.* **114**, 326 (1995).
5. Iyi, N., Inoue, Z., Takekawa, S., and Kimura, S., *J. Solid State Chem.* **52**, 66 (1984).
6. Iyi, N., Inoue, Z., Takekawa, S., and Kimura, S., *J. Solid State Chem.* **60**, 41 (1985).
7. Smets, B. M. J., and Verlijsdonk, J. G., *Mat. Res. Bull.* **21**, 1305 (1986).
8. Barklie, R. C., and O'Donnell, K., *J. Phys. C: Solid State Phys.* **10**, 4127 (1977).
9. Colomban, Ph., and Vivien, D., *Phys. Stat. Sol.* **76**, 565 (1983).
10. Laville, F., Gourier, D., Lejus, A. M., and Vivien, D., *J. Solid State Chem.* **49**, 180 (1983).
11. Gasperin, M., Saine, M. C., Kahn, A., Laville, F., and Lejus, A. M., *J. Solid State Chem.* **54**, 61 (1984).
12. Eguchi, K., Inoue, H., Sekizawa, K., and Arai, H., *Stud. Surf. Sci. Catal.* **101**, 417 (1996).
13. Groppi, G., Bellotto, M., Cristiani, C., Forzatti, P., and Villa, P. L., *Appl. Catal. A: General* **104**, 101 (1993).
14. Larson, A. C., and Von Dreele, R. B., Document LAUR 86-748, Los Alamos Laboratory, 1995.
15. Cromer, D. L., *Acta Cryst.* **18**, 17 (1965).
16. Manceau, A., Gorshkov, A. I., and Drits, V. A., *Am. Mineral* **77**, 1133 (1992).
17. Kohn, S. C., Charnock, J. M., Henderson, C. M. B., and Greaves, G. N., *Contrib. Mineral. Petrol.* **105**, 359 (1990).
18. Brow, G. E., Jr., Calas, G., Waychunas, G. A., and Petian, J., *Rev. mineral.* **18**, 431 (1988).
19. Wilkinson, A. P., Cheetam, A. K., and Cox, D. E., *Acta Cryst. B* **47**, 155 (1991).
20. Warner, J. K., Cheetham, A. K., Cox, D. E., and Von Dreele, R. B., *J. Am. Chem. Soc.* **114**, 6074 (1992).
21. Artioli, G., Pavese, A., Bellotto, M., Collins, S. P., and Lucchetti, G., *Am. Mineral.* **81**, 63 (1996).
22. Groppi, G., Cristiani, C., Forzatti, P., and Bellotto, M., *J. Mat. Sci.* **29**, 3441 (1994).